Supporting Information for "The Intrinsic 150-day Periodicity of the Southern Hemisphere Extratropical Large-Scale Atmospheric Circulation"

Sandro W. Lubis[1] * and Pedram Hassanzadeh[1]

[1]Rice University, Houston, TX, 77005, USA

Contents of this file

1. Text 1 to 6
2. Figures S1 to S7
3. Tables S1 to S4

---

*Current address: Pacific Northwest

National Laboratory, Richland, WA, 99354,

USA

1. Calculation of Feedback Strengths b_{ij} from Data

The feedback strengths in the coupled EOF1-EOF2 reduced-order model (Eqs. (4)-(5)) are estimated using the method introduced in Lubis and Hassanzadeh (2021), which is based on the lagged-regression method of Simpson, Shepherd, Hitchcock, and Scinocca (2013). We first define $reg_\ell(x(t), y(t)) = sum(x(t+\ell)y(t))$ for any time-series $x(t)$ and $y(t)$ and a time lag ℓ. As discussed in the main text, $\tilde{m}_j$ is the random component of the eddy forcing, independent from the zonal-mean flow, i.e., independent from z_1 or z_2 (Simpson et al., 2013). Therefore, $reg_\ell(\tilde{m}_j, z_k) \approx 0$ (for j,k=1,2) at positive lags ℓ longer than eddy lifetime (note that positive lags mean z_k leads). To find the values of b_{11} and b_{12}, each term in the linear feedback equation $m_1 = \tilde{m}_1 + b_{11}z_1 + b_{12}z_2$ is lag-regressed, at some positive lag $\ell > 7$ days, onto z_1 and then separately onto z_2, to arrive at the linear, coupled system

$$\begin{bmatrix} reg_\ell(z_1,z_1) & reg_\ell(z_2,z_1) \\ reg_\ell(z_1,z_2) & reg_\ell(z_2,z_2) \end{bmatrix} \begin{bmatrix} b_{11} \\ b_{12} \end{bmatrix} = \begin{bmatrix} reg_\ell(m_1,z_1) \\ reg_\ell(m_1,z_2) \end{bmatrix} \tag{1}$$

where $reg_\ell(\tilde{m}_1, z_1) \approx 0$ and $reg_\ell(\tilde{m}_1, z_2) \approx 0$ are used. Similarly, we lag-regressed each term in the linear feedback equation $m_2 = \tilde{m}_2 + b_{21}z_1 + b_{22}z_2$ onto z_1 and then z_2, to obtain

$$\begin{bmatrix} reg_\ell(z_1,z_1) & reg_\ell(z_2,z_1) \\ reg_\ell(z_1,z_2) & reg_\ell(z_2,z_2) \end{bmatrix} \begin{bmatrix} b_{21} \\ b_{22} \end{bmatrix} = \begin{bmatrix} reg_\ell(m_2,z_1) \\ reg_\ell(m_2,z_2) \end{bmatrix}. \tag{2}$$

In the method introduced in Simpson et al. (2013) for the single-EOF1 model LH01, $b_{12} = 0$, therefore, b_{11} can be computed directly from $reg_\ell(z_1, z_1)$ and $reg_\ell(m_1, z_1)$. Here, we solve the system of equations (S1) to find b_{11} and b_{12}. Similarly, the system of equations (S2) is solved to find b_{21} and b_{22}.

The proper time lag ℓ to use in Eqs. (S1)-(S2) should be chosen by looking for non-zero m_j z_k cross-correlations at positive lags beyond eddy lifetime. Simpson et al. (2013) suggested to average b_{11} values computed over a range of ℓ longer than the synoptic

timescale, which was also used by Lubis and Hassanzadeh (2021) for b_{jk}. Here, in an approach similar to the one used by Nie, Zhang, Chen, Yang, and Burrows (2014) and to provide uncertainties for estimates of b_{jk}, we compute a distribution of b_{jk} by averaging the values obtained for $\ell = \ell_i$ to $\ell = \ell_i + \Delta\ell \leq \ell_o$ where $\Delta\ell = 1, 2 \ldots 8$ days, and ℓ_i and ℓ_o are chosen for each model/dataset based on where cross-correlations become zero at small ($\sim 7 - 8$ days) and large ($\sim 15 - 20$ days) lag times. Table 2 of the paper reports the mean and 25th and 75th percentiles of each b_{jk} distribution and the range of ℓ_i to ℓ_o for ERA5, two setups of the idealized GCM, and CESM-WACCM. In all cases, the 25th-75th percentiles range is fairly narrow, indicating weak sensitivity to ℓ.

It is worth mentioning that all methods proposed in the literature for estimating eddy-zonal flow feedbacks from data have at least one free parameter such as ℓ; this includes the spectral methods of Lorenz and Hartmann (2001) and Ma, Hassanzadeh, and Kuang (2017). However, the latter study showed, using a test case for which the true feedback strength was known through the linear response function method of Hassanzadeh and Kuang (2019), that the sensitivity of the calculated feedback strengths to reasonable choices of these free parameters was weak in the methods of Lorenz and Hartmann (2001), Simpson et al. (2013), and Ma et al. (2017), consistent with what is found here.

Finally, it should be pointed out that in the reanalysis data, Lubis and Hassanzadeh (2021) found b_{13} and b_{23} to be small and statistically insignificant, indicating that EOF3 does not exert feedbacks onto EOF1 or EOF2 and is uncoupled from them. Therefore, the coupled EOF1-EOF2 model (Eqs. (4)-(5)) is enough for the current Southern Hemisphere large-scale circulation.

2. Analytical Solution of the Coupled EOF1-EOF2 Reduced-Order Model, Eqs. (4)-(5)

The analytical solution of the coupled system Eqs. (4)-(5) in the deterministic limit is discussed in detail in Lubis and Hassanzadeh (2021). Briefly, we set $\tilde{m}_j = 0$ and re-write the equations as a system of ordinary differential equations (ODEs) in the matrix form:

$$\dot{\mathbf{z}} = \mathbf{A}\mathbf{z}, \tag{3}$$

where

$$\mathbf{z} = \begin{bmatrix} z_1 \\ z_2 \end{bmatrix}, \tag{4}$$

$$\mathbf{A} = \begin{bmatrix} b_{11} - \frac{1}{\tau_1} & b_{12} \\ b_{21} & b_{22} - \frac{1}{\tau_2} \end{bmatrix}. \tag{5}$$

The solution of this system is

$$\mathbf{z} = c_1 e^{\lambda_1 t}\mathbf{v}_1 + c_2 e^{\lambda_2 t}\mathbf{v}_2, \tag{6}$$

where $\mathbf{v}$ and λ are the eigenvectors and the eigenvalues of matrix $\mathbf{A}$, respectively, and c_1 and c_2 are some constants that depend on the initial conditions. The eigenvalues λ of $\mathbf{A}$ are

$$\lambda_{1,2} = -\frac{1}{2}\left(\frac{1}{\tau_1} + \frac{1}{\tau_2} - b_{11} - b_{22}\right) \pm \frac{1}{2}\sqrt{\left\{\left(\frac{1}{\tau_1} - \frac{1}{\tau_2}\right) - (b_{11} - b_{22})\right\}^2 + 4b_{12}b_{21}}. \tag{7}$$

It is clear from Eq. (S7) that whether Eqs. (4)-(5) admit purely decaying or decaying-oscillatory solutions depends on the sign of the term under the square root, leading to the criterion in Eq. (6).

If Eq. (6) is not satisfied, then there is no oscillation and z just decays exponentially according to

$$\mathbf{z} = c_1 e^{(-\sigma_1 t)}\mathbf{v}_1 + c_2 e^{(-\sigma_2 t)}\mathbf{v}_2. \tag{8}$$

where $\sigma_{1,2} = -\lambda_{1,2} > 0$ are the decay rates. This solution corresponds to the non-propagating annular modes and is characterized by overly persistent and dominant z_1

(see Lubis and Hassanzadeh (2021) for more details). If Eq. (6) is satisfied, then a decaying-oscillatory solution of the form

$$\mathbf{z} = c_1 e^{(-\sigma t)} e^{(i\omega t)} \mathbf{v}_1 + c_2 e^{(-\sigma t)} e^{(-i\omega t)} \mathbf{v}_2 \tag{9}$$

exists, where decay rate σ (Eq. (S10)) and oscillation frequency ω (Eq. (7)) are the real and imaginary parts of $\lambda_{1,2} = -\sigma \pm i\omega$ from Eq. (S7):

$$\sigma = \frac{1}{2}\left(\frac{1}{\tau_1} + \frac{1}{\tau_2} - b_{11} - b_{22}\right), \tag{10}$$

This solution corresponds to the propagating annular modes and is characterized by strongly coupled z_1 and z_2 of comparable persistence and dominance (see Lubis and Hassanzadeh (2021)). Note that under the reasonable simplification $\tau_1 \approx \tau_2$ (see Table 2), the criterion in Eq. (6) reduces to $(b_{11} - b_{22})^2 < -4b_{12}b_{21}$ as the necessary and sufficient condition for the existence of the propagating regime. It is clear from this equation (or from Eq. (6)) that a necessary (but not sufficient) condition is

$$b_{12}b_{21} < 0. \tag{11}$$

Equation (S11) shows that non-zero cross-EOF feedbacks of opposite sign are necessary for the propagating regime, a condition that is clearly satisfied in ERA5, idealized GCM with propagating regime, and CESM-WACCM (Table 2).

3. Spectral Analysis of Time-Series

For the spectral analyses in Figs. 1, 3, S1 and S2, we divide the time-series into 1052-day segments that overlap by 500 days and are windowed by a Hanning window (Lorenz & Hartmann, 2001; Ma et al., 2017). With this approach, the spectral estimates in Figs. 1a, 1b, 1c, and 1d (black curves) have ∼29, ∼190, ∼190 and ∼190 degrees of freedom, respectively. To test the statistical significance of each spectrum, the "red-noise" spectral

estimate $P_{red}\ (f)$ at frequency f is calculated as:

$$P_{red}(f) = \frac{\sigma^2(1-R^2)}{1+R^2-2R\cos(2\pi f)}, \tag{12}$$

where R is the lag-1 autocorrelation coefficient of the time-series and σ^2 is the variance (Jenkins, 1968). Prior to the spectral analysis, the anomalies are detrended to remove a linear trend, and smoothed using a 21-day centered moving average to avoid high-frequency noises, similar to Sheshadri and Plumb (2017). As a result, the red noise would shift from the centroid of the spectru because of the filtered anomaly field (see Fig. 2 in Ventrice et al. (2013) for a similar example).

In Fig. S1, sensitivity of the zonal index z_1 power spectrum to different choices of time period, segment length, and overlap are examined. While there is some sensitivity at higher frequencies, the $\sim$ 150 day peak is overall robust. The main sensitivity is with respect to change in time period, but in all cases, the peak exists and its timescale agrees with the theoretical prediction periodicity.

4. Stochastic Prototype

In Fig. S4, synthetic data from numerical integrations of a stochastic prototype is presented. The prototype is presented in detail in Lubis and Hassanzadeh (2021). Briefly, the stochastic prototype consists of Eqs. (4)-(5) with time-series $\tilde{m}_1$ and $\tilde{m}_2$ modeled as second-order autoregressive (AR2) noise processes, following Simpson et al. (2013), and values of τ_1, τ_2, b_{11}, b_{12}, b_{21}, and b_{22} prescribed (Table S2). For the control (CTL) experiment, these values are chosen close to the observed ones in the Southern Hemisphere. In the other three experiments, values of b_{12} and b_{21} are varied to change whether a propagating or non-propagating regime exists (based on Eq. (6)) or to change the periodicity of the propagation.

5. Bartlett Test: Standard Errors of Cross Correlations

The standard error of the estimated cross-correlation $r_{XY}(\ell)$ between two stationary normal time-series $\{X_t\}$ and $\{Y_t\}$ ($t \in [0 \quad T]$) at lag ℓ can be computed as (Bartlett, 1978)

$$\mathrm{var}\left\{r_{XY}(\ell)\right\} = \frac{1}{T-|\ell|}\sum_{g=-\infty}^{\infty}\left[\rho_X(g)\rho_Y(g)\right], \tag{13}$$

where $\rho_X(g)$ and $\rho_Y(g)$ are the autocorrelation function of $\{X_t\}$ and $\{Y_t\}$, respectively. The null hypothesis is $r_{XY}(\ell) = 0$, and it is rejected at the 5% significance level if $|r_{XY}(\ell)| > 2 \times \sqrt{\mathrm{var}\left\{r_{XY}(\ell)\right\}}$.

6. One-point Lag-correlation Map

The one-point lag-correlation maps in Figs. 4-5 are computed following Son and Lee (2006). Briefly, we choose the position of the maximum negative wind anomalies of EOF2 at low latitudes as the base latitude. Then the Pearson's correlation coefficient between zonal-mean zonal wind anomalies at lag time l and latitude ϕ are computed with respect to the zonal-mean zonal wind anomalies at the base latitude.

References

Bartlett, M. S. (1978). An introduction to stochastic processes with special reference to methods and applications. *Journal of the Institute of Actuaries*, *81*(2), 198–199. doi: 10.1017/S0020268100035964

Hassanzadeh, P., & Kuang, Z. (2019, 04). Quantifying the annular mode dynamics in an idealized atmosphere. *Journal of the Atmospheric Sciences*, *76*(4), 1107-1124. doi: 10.1175/JAS-D-18-0268.1

Jenkins, G. M. (1968). Spectral analysis and its applications. *Holden-Day, Inc., San Francisco, Card Nr. 67-13840*.

Lorenz, D. J., & Hartmann, D. L. (2001, 11). Eddy-zonal flow feedback in the Southern Hemisphere. *Journal of the Atmospheric Sciences*, *58*(21), 3312-3327. doi: 10.1175/1520-0469(2001)058<3312:EZFFIT>2.0.CO;2

Lubis, S. W., & Hassanzadeh, P. (2021). An eddy-zonal flow feedback model for propagating annular modes. *Journal of the Atmospheric Sciences*, *78*(1), 249 - 267. Retrieved from `https://journals.ametsoc.org/view/journals/atsc/78/1/jas-d-20-0214.1.xml` doi: 10.1175/JAS-D-20-0214.1

Ma, D., Hassanzadeh, P., & Kuang, Z. (2017, 01). Quantifying the Eddy–Jet Feedback Strength of the Annular Mode in an Idealized GCM and Reanalysis Data. *Journal of the Atmospheric Sciences*, *74*(2), 393-407. doi: 10.1175/JAS-D-16-0157.1

Nie, Y., Zhang, Y., Chen, G., Yang, X.-Q., & Burrows, D. A. (2014). Quantifying barotropic and baroclinic eddy feedbacks in the persistence of the southern annular mode. *Geophysical Research Letters*, *41*(23), 8636-8644. doi: 10.1002/2014GL062210

Sheshadri, A., & Plumb, R. A. (2017, 04). Propagating annular modes: empirical orthogonal functions, principal oscillation patterns, and time scales. *Journal of the*

Atmospheric Sciences, *74*(5), 1345-1361. doi: 10.1175/JAS-D-16-0291.1

Simpson, I. R., Shepherd, T. G., Hitchcock, P., & Scinocca, J. F. (2013). Southern annular mode dynamics in observations and models. part ii: Eddy feedbacks. *Journal of Climate*, *26*(14), 5220 - 5241. Retrieved from `https://journals.ametsoc.org/view/journals/clim/26/14/jcli-d-12-00495.1.xml` doi: 10.1175/JCLI-D-12-00495.1

Son, S.-W., & Lee, S. (2006, 05). Preferred Modes of Variability and Their Relationship with Climate Change. *Journal of Climate*, *19*(10), 2063-2075. doi: 10.1175/JCLI3705.1

Son, S.-W., Lee, S., Feldstein, S. B., & Ten Hoeve, J. E. (2008, 03). Time scale and feedback of zonal-mean-flow variability. *Journal of the Atmospheric Sciences*, *65*(3), 935-952. doi: 10.1175/2007JAS2380.1

Ventrice, M. J., Wheeler, M. C., Hendon, H. H., Schreck, C. J., Thorncroft, C. D., & Kiladis, G. N. (2013). A modified multivariate madden–julian oscillation index using velocity potential. *Monthly Weather Review*, *141*(12), 4197 - 4210. doi: 10.1175/MWR-D-12-00327.1

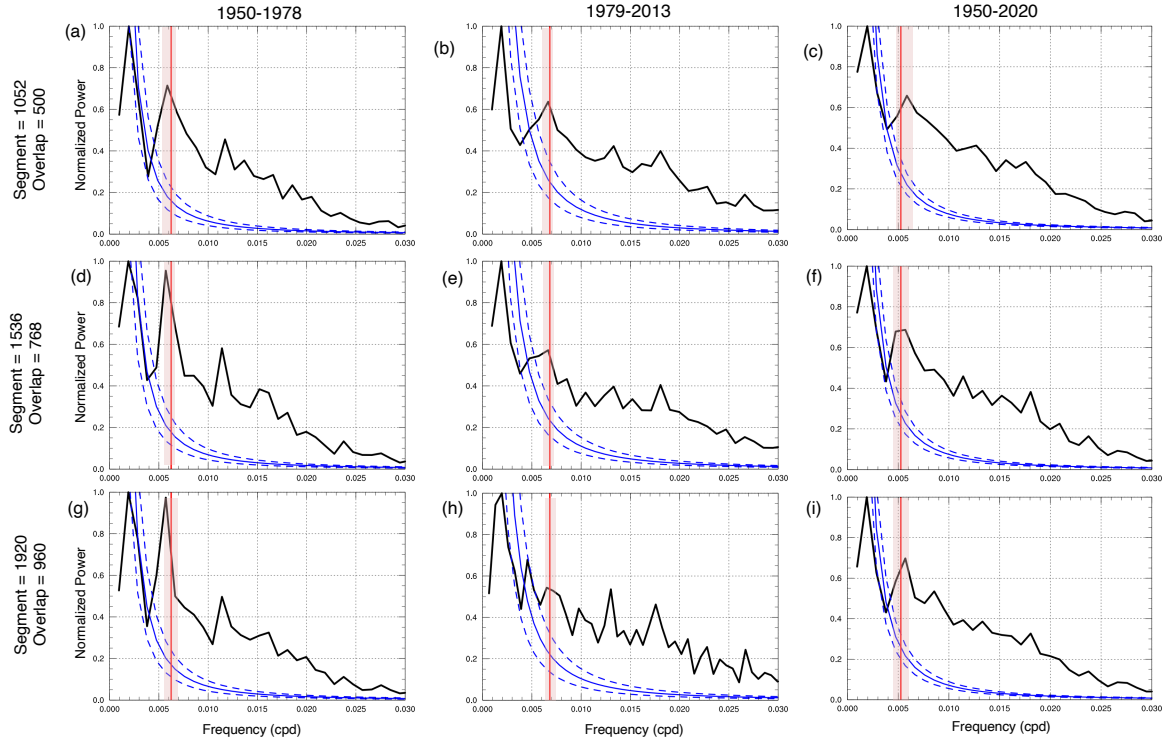

Figure S1. Periodicity in the Southern Annular Mode (SAM) in ERA5 reanalysis with respect to various changes in the methodology: different time periods (1950-1978, 1979-2013, and 1950-2020), different window lengths (1052, 1536, and 1920 days), and different overlaps (500, 768, and 960 days). See the caption of Fig. 1 for more details. Overall, the observed 150-day periodicity is robust across various changes in the methodology and is well predicted by the reduced-order model (Eq. (7)). Change in the predicted periodicity is due to slight changes in the strength of the feedbacks in different periods (not shown).

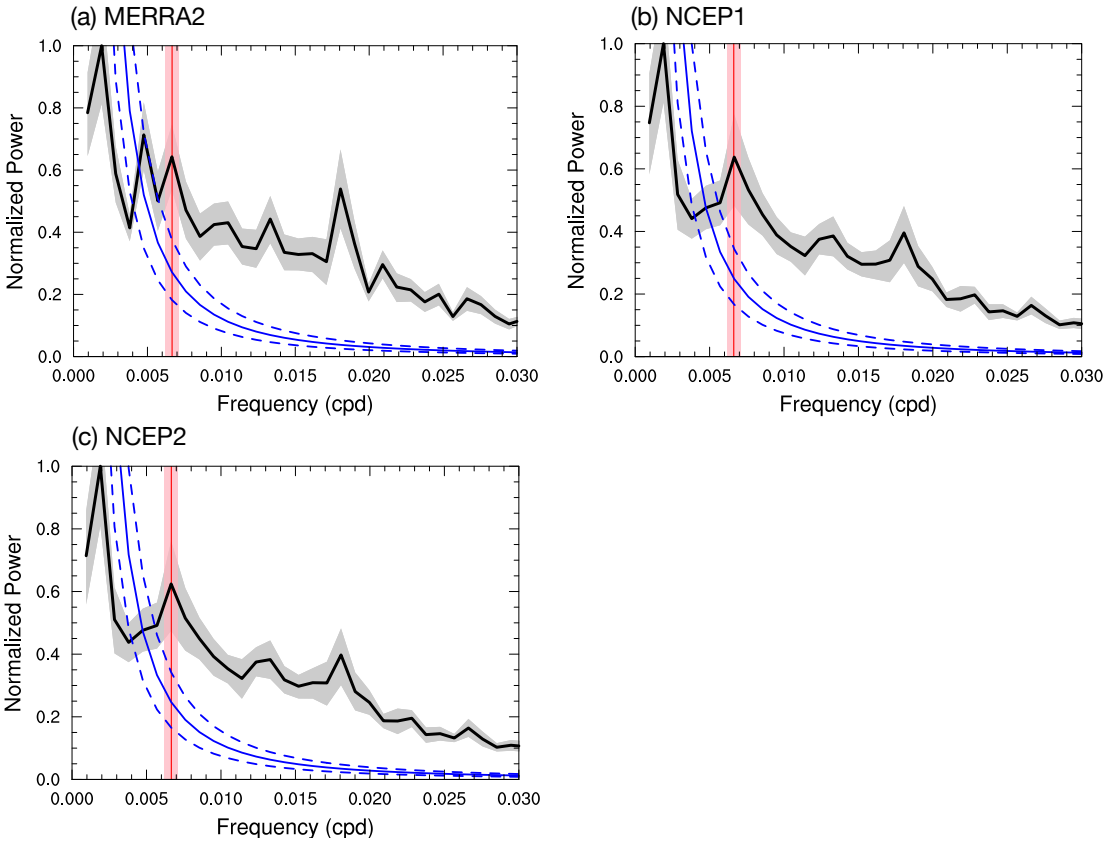

Figure S2. Periodicity in the Southern Annular Model (SAM) of three other reanalysis products. Same as Fig. 1 but for (a) MERRA2, (b) NCEP1, and (c) NCEP2. See Table S1 for the mean and 25th to 75th percentiles of the theoretically predicted frequency distribution from Eq. (7). See Materials and Methods for more information about each reanalysis dataset and the spectral analysis of time-series.

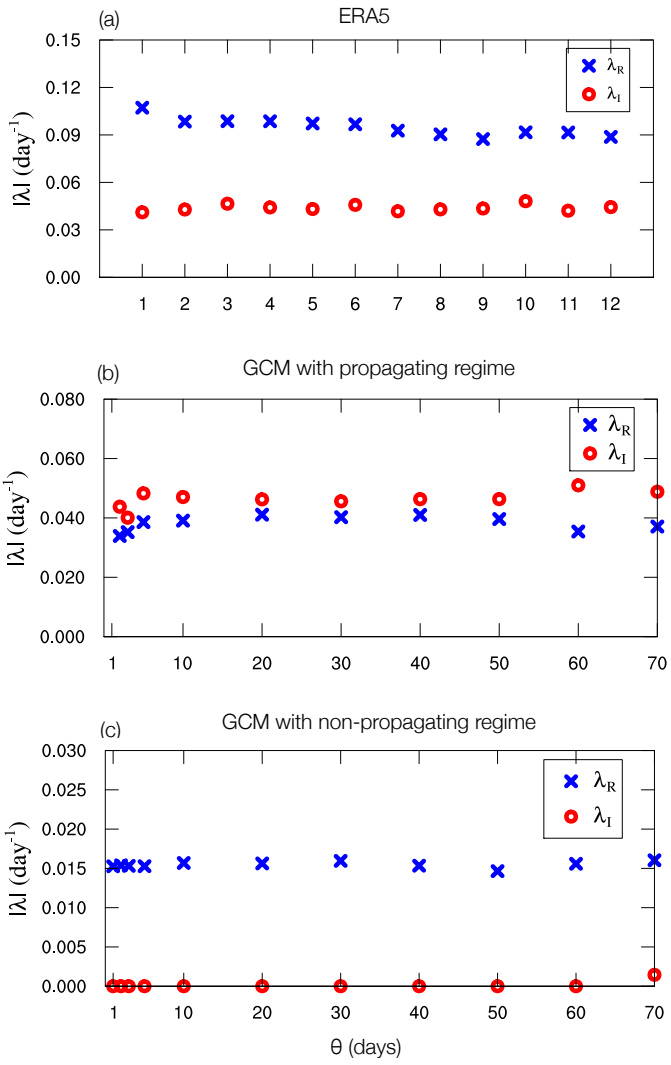

Figure S3. Dependence of the calculated eigenvalues λ of the leading POP/DMD modes on the choice of time lag θ. (a) ERA5, (b) idealized GCM with the propagating regime, and (c) idealized GCM with the non-propagating regime. Longer time lags are tested in the idealized GCM given the abundance of data and longer zonal index autocorrelation times.

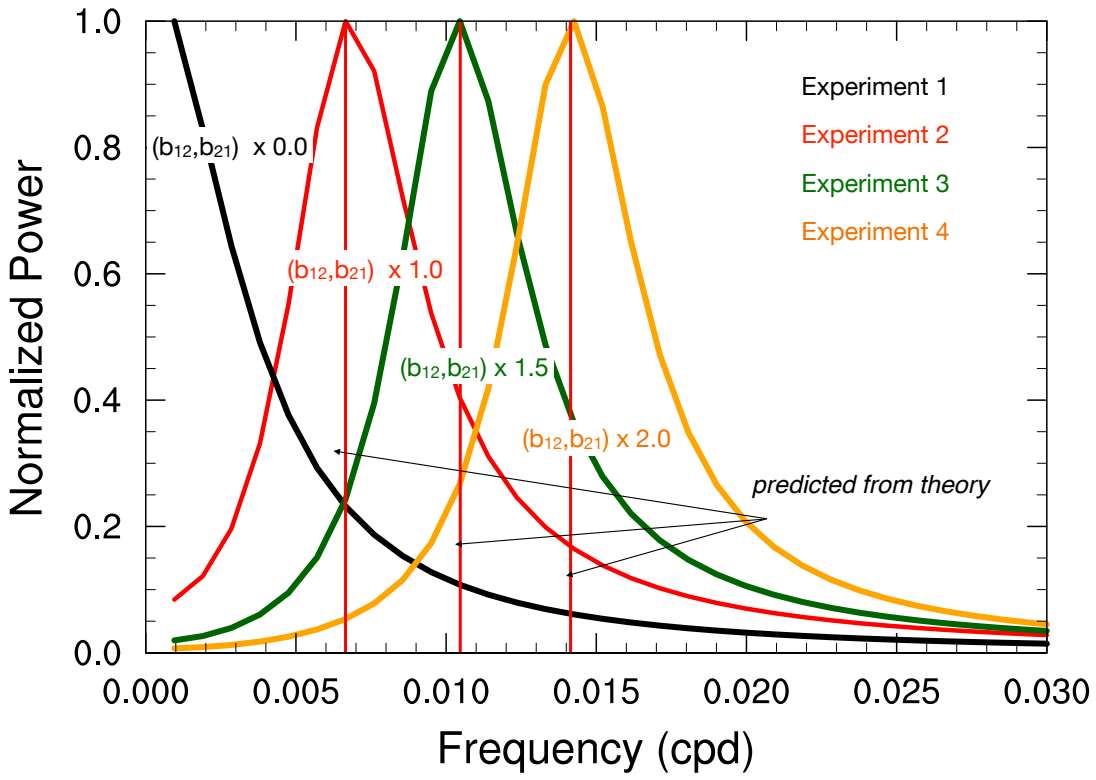

Figure S4. Power spectra of z_1 from synthetic data of the stochastic prototypes for different combinations of cross-feedbacks (b_{12} and b_{21} relative to those in the Control experiment are changed; see Table S2). The thin vertical lines mark the theoretically predicted frequency from Eq. (7). For all cases shown in this figure, except for panel (c) and the black line in panel (d), the criterion for the existence of the propagating annular mode (Eq. (6)) is satisfied and Eq. (7) accurately predicts the periodicity.

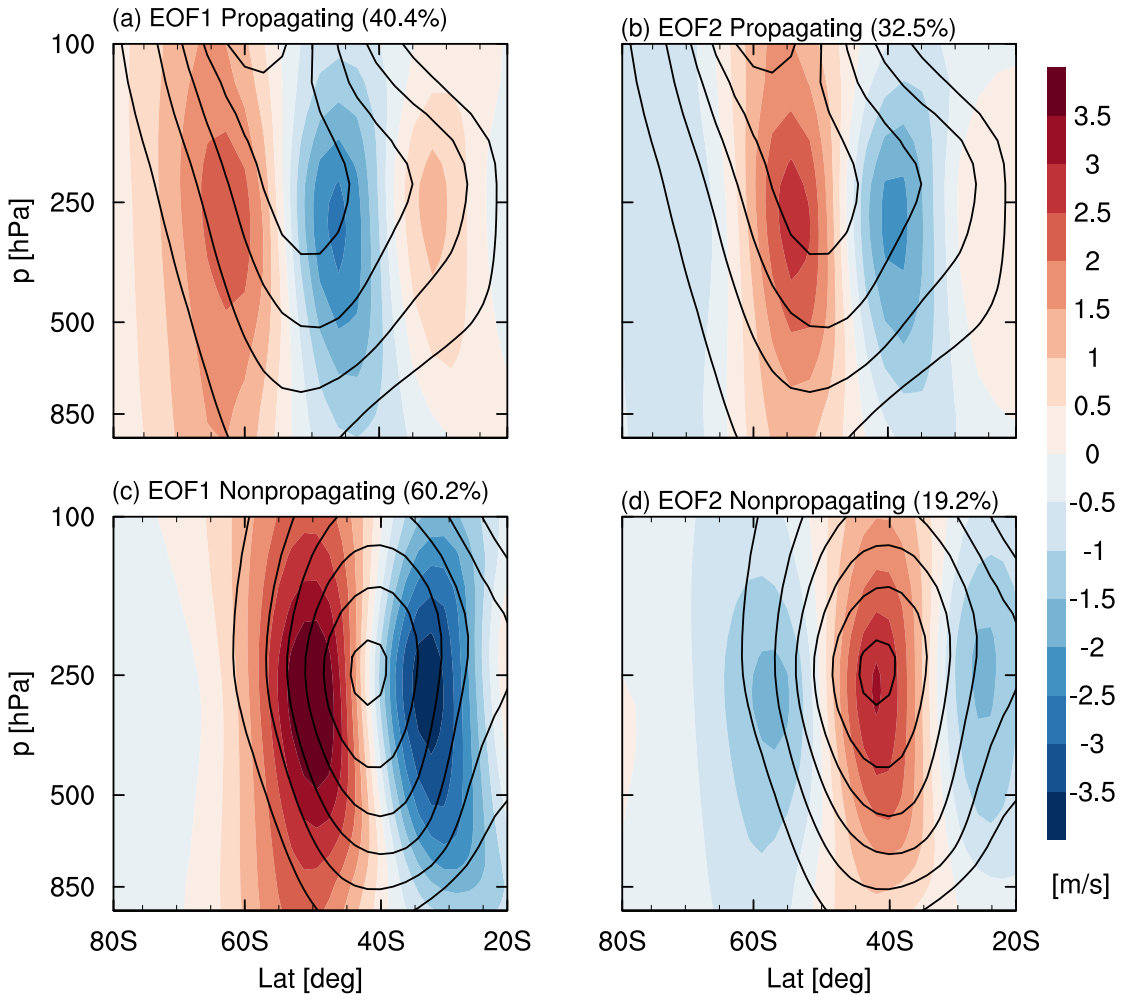

Figure S5. Patterns of EOF1, EOF2, and zonal-mean zonal wind climatology in two setups of an idealized GCM. (a)-(b) Setup with the propagating regime. (c)-(d) Setup with the non-propagating regime. Shading shows the EOF patterns, which are obtained by regressing the Southern Hemisphere daily zonal-mean zonal wind onto z_1 (PC1, left) and z_2 (PC2, right). The contour lines show the climatological zonal-mean zonal wind with an interval of 5 m/s. Numbers in the parentheses show the variance explained by each EOF. The ratio of EOF1/EOF2 explained variances and the climatological jet structure in (a)-(b), but not in (c)-(d), are consistent with the rule of thumb for the existence of the propagating regime of annular modes: ratio <2 and double jet are associated with the propagating regime (Son & Lee, 2006; Son et al., 2008). See Materials and Methods for details of each idealized GCM setup and the EOF analysis.

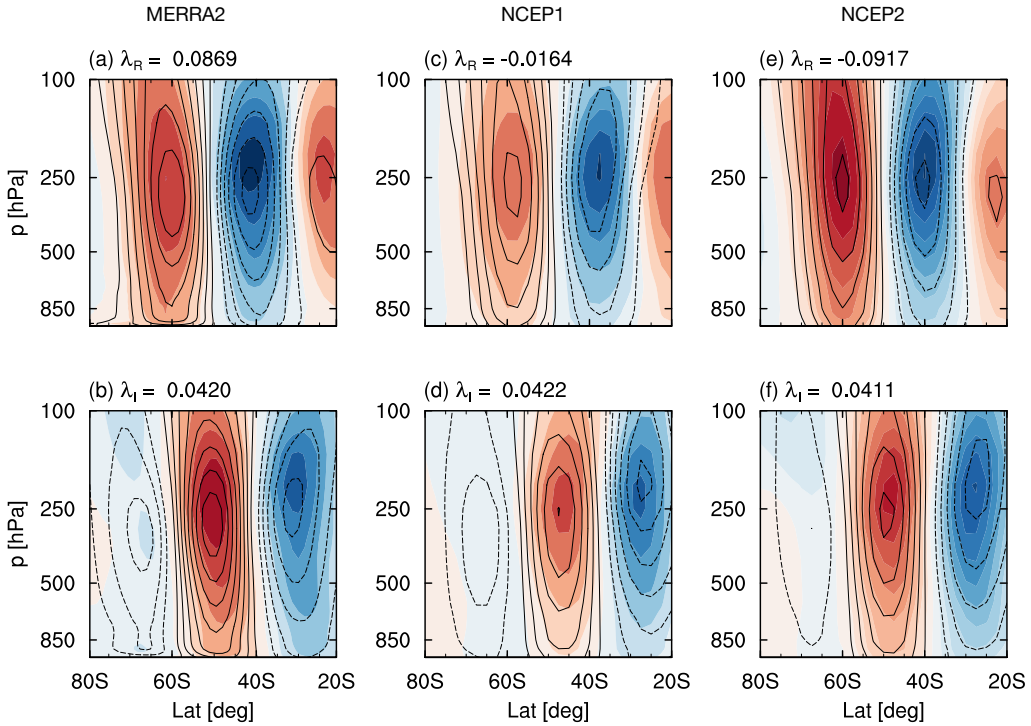

Figure S6. Periodicity in the dynamical modes of the zonal-mean Southern Hemisphere extratropical large-scale circulation. Same as Fig. 2 but for year-round MERRA2 (a)-(b), NCEP1 (c)-(d), and NCEP2 (e)-(f). Periodicity of each mode is $2\pi/\lambda_I$ ∼150 days. Periodicity of the leading POP/DMD mode in each dataset closely matches the theoretically predicted ones through Eq. (7); see Table S1. See Materials and Methods for more information about each reanalysis dataset and the POP/DMD calculations.

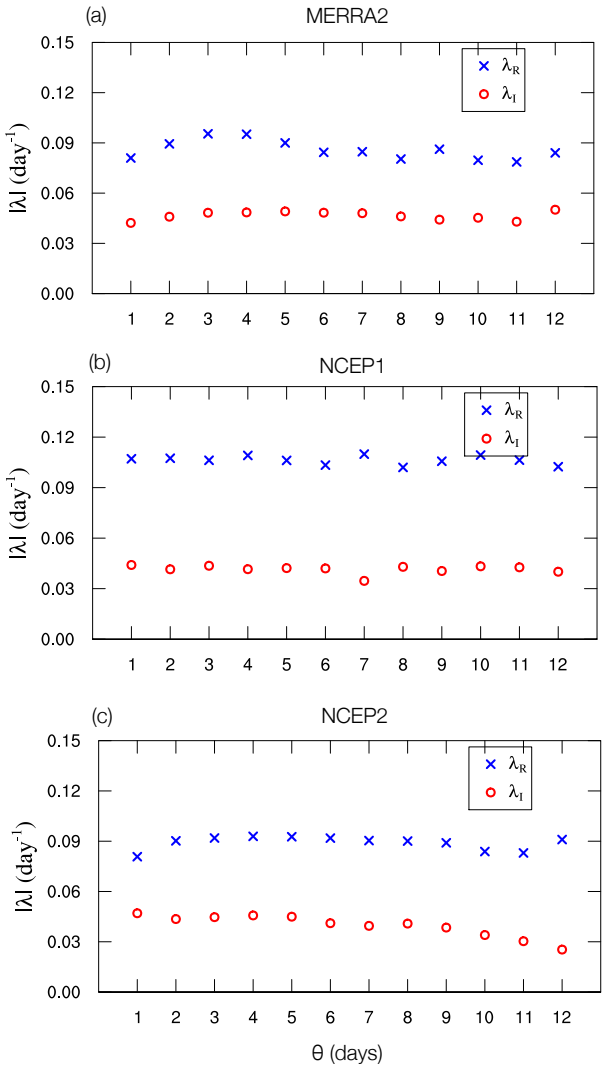

Figure S7. Dependence of the calculated eigenvalues λ of the leading POP/DMD modes on the choice of time lag θ. (a) MERRA2, (b) NCEP1, and (c) NCEP2.

Table S1. Periodicity of SAM in three other reanalysis datasets: MERRA2, NCEP1, and NCEP2. The second column shows the periodicity predicted by the theoretically derived Eq. (7) given the estimates of b_{jk} and τ_j from data. The 25th and 75th percentiles provide a measure of the uncertainty with respect to the choice of lag time l in estimating b_{jk} (see Materials and Methods). The third column shows the periodicity associated with the peak of z_1 spectrum in Figs. S2a-c. The last column shows the periodicity of the leading POP/DMD mode, computed as $2\pi/\lambda_I$, where λ_I is the imaginary part of the eigenvalue (Eq. (A9)). See Appendix for more details about the POP/DMD calculations.

Data	Periodicity predicted by Eq. (7) (25^{th}, mean,75^{th}) (days)	Periodicity at the peak of z_1 spectrum (days)	Periodicity of the leading POP/DMD mode (days)
MERRA2	(143.2, 150.1, 155.5)	150.3	149.5
NCEP1	(141.5, 151.8, 157.8)	150.3	148.8
NCEP2	(141.8, 149.8, 156.5)	150.3	152.8

Table S2. Feedback strengths and damping timescales prescribed in 4 numerical experiments with the stochastic prototypes to produce the synthetic data for Fig. 1d. See Materials and Methods for details of the stochastic prototype. In all experiments, τ_1=τ_2=8 days is used. The b_{jk} values for the control (CTL) experiment are chosen close to the observed ones (Table 2). Next to the last column shows the periodicity at the peak of z_1 specrum in Fig. 1d for each experiment. The last column shows the periodicity predicted by the theoretically derived Eq. (7) for the given values of b_{jk} and τ_j. Experiment 4 is in the non-propagating regime, i.e., the criterion in Eq. (6) is not satisfied (simply because b_{12} b_{21}=0).

Data	Prescribed feedback strengths (day^{-1})				Periodicity at the peak of z_1 spectrum (day)	Periodicity predicted by Eq. (7) (day)
	b_{11}	b_{12}	b_{21}	b_{22}		
Experiment 1 (CTL)	0.0485	0.0737	-0.0277	0.0142	150.3	149.2
Experiment 2	0.0485	CTL×1.5	CTL×1.5	0.0142	95.6	95.5
Experiment 3	0.0485	CTL×2.0	CTL×2.0	0.0142	70.1	70.7
Experiment 4	0.0485	0.0	0.0	0.0142	-	-

Table S3. List of 24 Coupled Model Intercomparison Project Phase 5 (CMIP5) models used in this study. We use all available ensemble members from CMIP5 historical simulations for the period 1960-2005 for Figs. 6-7.

Model #	Institution	Model	Experiment	Atmospheric Model Resolution (Lon x Lat)
1	BCC	bcc-csm1-1-m	historical	1.59° x 1.59°
2		bcc-csm1-1	historical	3.96° x 3.96°
3	BNU	BNU-ESM	historical	3.96° x 3.96°
4	CCCma	CanESM2	historical	2.81° x 2.81°
5	NCAR	CCSM4	historical	1.25° x 0.94°
6	CMCC	CMCC-CM	historical	1.06° x 1.06°
7		CMCC-CMS	historical	2.64° x 2.64°
8	CNRM-CERFACS	CNRM-CM5	historical	1.98° x 1.98°
9	CSIRO-QCCCE	CSIRO-Mk3-6-0	historical	1.93° x 1.93°
10	LASG-CESS	FGOALS-g2	historical	2.81° x 2.81°
11	NOAA-GFDL	GFDL-CM3	historical	2.50° x 2.00°
12		GFDL-ESM2G	historical	2.50° x 2.00°
13		GFDL-ESM2M	historical	2.50° x 2.00°
14	MOHC	HadGEM2-CC	historical	2.25° x 2.25°
15		HadCM3	historical	2.50° x 3.75°
16	INM	INM-CM4	historical	2.00° x 1.50°
17	MIROC	MIROC-ESM	historical	2.81° x 2.81°
18		MIROC-ESM-CHEM	historical	3.96° x 3.96°
19	MPI-M	MPI-ESM-LR	historical	1.88° x 1.87°
20		MPI-ESM-MR	historical	1.88° x 1.87°
21		MPI-ESM-P	historical	1.88° x 1.87°
22	MRI	MRI-CGCM3	historical	1.59° x 1.59°
23		MRI-ESM1	historical	1.59° x 1.59°
24	NCC	NorESM1-M	historical	2.50° x 1.89°

Table S4. List of 20 Coupled Model Intercomparison Project Phase 6 (CMIP6) models used in this study. We use all available ensemble members from CMIP6 historical simulations for the period 1960-2005 for Figs. 6-7.

Model #	Institution	Model	Experiment	Atmospheric Model Resolution (Lon x Lat)
1	CSIRO-ARCCSS	ACCESS-ESM1-5	historical	2.25° x 2.25°
2	BCC	BCC-CSM2-MR	historical	1.13° x 1.13°
3		BCC-ESM1	historical	2.81° x 2.81°
4	CAMS	CAMS-CSM1-0	historical	1.13° x 1.13°
5	CCCma	CanESM5	historical	2.81° x 2.81°
6	NCAR	CESM2-WACCM	historical	1.25° x 0.94°
7	CNRM-CERFACS	CNRM-CM6-1	historical	1.40° x 1.40°
8		CNRM-ESM2-1	historical	1.40° x 1.40°
9	NOAA-GFDL	GFDL-CM4	historical	1.25° x 1.00°
10	NASA-GISS	GISS-E2-1-G	historical	2.50° x 2.00°
11	MOHC	HadGEM3-GC31-LL	historical	1.88° x 1.25°
12	INM	INM-CM5-0	historical	2.50° x 2.50°
13	IPSL	IPSL-CM6A-LR	historical	2.50° x 1.26°
14	NIMS-KMA	KACE-1-0-G	historical	1.88° x 1.25°
15	MIROC	MIROC6	historical	1.98° x 1.98°
16		MIROC-ES2L	historical	2.80° x 2.80°
17	MPI-M	MPI-ESM1-2-LR	historical	1.88° x 1.87°
18	MRI	MRI-ESM2-0	historical	1.59° x 1.59°
19	NCC	NorESM2-LM	historical	2.50° x 1.88°
20	MOHC	UKESM1-0-LL	historical	1.88° x 1.25°